

**FORMATION OF NANOTUBULAR OXIDE BY ANODIZATION
OF VALVE METALS**

SYAHRIZA BT ISMAIL

UNIVERSITI SAINS MALAYSIA

2013

DECLARATION

I hereby declare that I have conducted, completed the research work and written the thesis entitles “Formation of Nanotubular Oxide by Anodization of Valve Metals”. I also declare that it has not been previously submitted for the award of any degree or diploma or other similar title of this for any other examining body or university.

Name of Student: Syahriza Ismail

Signature:

Date:

Witness by

Supervisor: Assoc. Prof. Dr. Zainovia Lockman

Signature:

Date:

ACKNOWLEDGMENT

In the name of Allah, the Most Gracious and the Most Merciful

Alhamdulillah, all praises to Allah for the strengths and His blessing in completing this thesis. It would not have been possible without the guidance and the help of several individuals who in one way or another contributed and extended their valuable assistance in the preparation and completion of this study.

First and foremost, my utmost gratitude goes to my supervisor Assoc. Prof. Dr. Zainovia Lockman for her supervision and constant support. Her invaluable help of constructive comments and suggestions throughout the experimental and thesis works have contributed to the success of this research. Not forgotten, my appreciation to my co-supervisor, Prof. Zainal Arifin Ahmad for his support and understanding regarding this works.

I am deeply thankful to USM for giving me the opportunity of being a postgraduate student in School of Materials & Mineral Resources Engineering. My sincere thanks to Dean, Deputy Deans, lecturers, technicians, staff and others whose contributed in my study. Thank you to KPT and UTEM, for financial support. Special thanks to my fellow friends especially Nazida, Dr. Umar and GEMs group members (Azhar, Miftah, Mona and Ehsan) that is always willing to help when I encountered difficulties. Thank you so much.

My never ending gratitude and loving thanks to my parents, Pn. Hj. Siti Hawa Tahir and my late father Hj. Ismail Awang, my brother, my sisters and their families. Without their encouragement and attentive it would have been impossible for me to complete this work. Last but not least, to everybody who has directly and indirectly involve in accomplishment of my study successfully, your cooperation is highly appreciate.

TABLE OF CONTENTS

DECLARATION.....	ii
ACKNOWLEDGMENT	iii
TABLE OF CONTENTS	iv
LIST OF TABLES	viii
LIST OF FIGURES.....	xi
LIST OF ABBREVIATIONS	xx
LIST OF SYMBOLS.....	xxi
ABSTRAK	xxii
ABSTRACT	xxiv
CHAPTER 1 - INTRODUCTION	1
1.1 Background.....	1
1.2 Problem statement	3
1.3 Research objectives	7
1.4 Thesis outline.....	8
CHAPTER 2 - LITERATURE REVIEW	9
2.1 Introduction	9
2.2 Valve metal oxide.....	9
2.2.1 Properties of transition (valve) metal oxide.....	9
2.2.1.1 Properties of TiO ₂	11
2.2.1.2 Properties of ZrO ₂	16
2.2.1.3 Properties of WO ₃	20
2.2.2 Anodic oxidation of transition (valve) metal oxides	22
2.2.3 Oxide breakdown.....	29
2.3 Metal oxide nanostructures.....	32
2.3.1 1-D oxide nanomaterials.....	34
2.3.2 Oxide nanotubes	36

2.4	Synthesis of 3-D network oxide formation by anodization.....	38
2.4.1	Self assembled 3-D nanoporous formation mechanism	40
2.4.2	Self assembled 3-D nanotubular formation mechanism.....	43
2.4.2.1	TiO ₂ nanotubes (TNTs)	48
2.4.2.2	ZrO ₂ nanotubes (ZNTs).....	51
2.4.2.3	WO ₃ nanoporous.....	57
CHAPTER 3 - METHODOLOGY		60
3.1	Introduction	60
3.2	Raw materials	61
3.3	Procedure of experiment and parameters studied.....	63
3.3.1	Anodization of Ti.....	67
3.3.1.1	Effect of electrolyte	68
3.3.1.2	Effect of annealing temperature	68
3.3.1.3	Effect of annealing time	69
3.3.1.4	Methyl orange degradation.....	69
3.3.2	Anodization of Zr	69
3.3.2.1	Anodization in aqueous Na ₂ SO ₄ electrolyte.....	70
3.3.2.2	Anodization in glycerol electrolyte	72
3.3.2.3	Anodization in ethylene glycol (EG).....	73
3.3.2.4	Anodization in EG with oxidant.....	75
3.3.2.5	Methyl orange degradation.....	77
3.3.3	Anodization of W	78
3.3.3.1	Effect of NH ₄ F loading in aqueous electrolyte.....	78
3.3.3.2	Effect of pH	79
3.3.3.3	The effect of anodization time.....	79
3.3.3.4	Methyl orange degradation.....	79
3.4	Characterization techniques.....	80
3.4.1	Field Emission Scanning Electron Microscopy (FESEM)	80
3.4.2	Energy Dispersive X-ray spectroscopy (EDX).....	81
3.4.3	X-ray Diffraction spectrometry (XRD)	81
3.4.4	Transmission Electron Microscopy (TEM).....	83
3.4.5	Raman spectroscopy	84
3.4.6	Photoluminescence (PL).....	85

3.4.7	UV-Visible.....	86
3.4.8	Energy Filtered Transmission Electron Microscopy (EFTEM)	86
CHAPTER 4 - RESULT AND DISCUSSION		88
4.1	Introduction	88
4.2	Experiment 1: Anodization of Ti.....	88
4.2.1	Effect of electrolyte	89
4.2.2	Mechanism of TNTs formation	95
4.2.3	Crystalline evolution in TNTs	99
4.2.3.1	Effect of annealing temperatures.....	100
4.2.3.2	Effect of annealing time	109
4.2.3.3	Photodegradation : Anodic TNTs.....	110
4.3	Experiment 2: Anodization of Zr	113
4.3.1	Anodization of Zr in aqueous electrolyte	119
4.3.1.1	Effect of voltage on the formation of ZNTs.....	119
4.3.1.2	Effect of anodization time on the formation of ZNTs... ..	141
4.3.1.3	Effect of NH ₄ F loading on the formation of ZNTs	144
4.3.1.4	Effect of annealing.....	149
4.3.1.5	Photodegradation: Anodic ZNTs in aqueous.....	155
4.3.1.6	Summarize of Zr anodized in aqueous electrolyte	157
4.3.2	Anodization of Zr in glycerol electrolyte	158
4.3.2.1	Effect of applied voltage on the formation of ZNTs	158
4.3.2.2	Effect of anodization time on the formation of ZNTs... ..	170
4.3.2.3	Effect of NH ₄ F loading on the formation of ZNTs	172
4.3.2.4	Effect of annealing.....	177
4.3.2.5	Photodegradation: Anodic ZNTs in glycerol.....	179
4.3.2.6	Summarize of Zr anodized in glycerol	181
4.3.3	Anodization of Zr in ethylene glycol (EG) electrolyte	181
4.3.3.1	Effect of applied voltage and NH ₄ F loading on the ZNTs formation.....	183
4.3.3.2	Effect of anodization time on the ZNTs formation	196
4.3.3.3	Effect of annealing.....	199
4.3.3.4	Photodegradation: Anodic ZNTs in EG	201
4.3.3.5	Summarize of Zr anodized in EG	203

4.3.4	Anodization of Zr in EG with oxidant.....	203
4.3.4.1	Anodization with H ₂ O addition.....	204
4.3.4.2	Anodization with H ₂ O ₂ addition.....	217
4.3.4.3	Photodegradation: Anodic ZNTs in EG + oxidant.....	226
4.4	Experiment 3: Anodization of W.....	228
4.4.1	Anodic oxidation of W in Na ₂ SO ₄	228
4.4.2	Formation mechanism of segmented WO ₃ nanotubes (WNTs) ..	232
4.4.3	Effect of pH for the formation of segmented WNTs.....	236
4.4.4	Effect of anodizing time for the formation of segmented WNTs	241
4.4.5	TEM image for WO ₃ anodized in optimized condition.....	243
4.4.6	Photodegradation: Anodic WNTs.....	244
4.4.7	Summarize of W anodized in Na ₂ SO ₄	245
CHAPTER 5 - CONCLUSION AND RECOMMENDATIONS		247
5.1	Conclusion.....	247
5.2	Recommendations	250
REFERENCES.....		251
LIST OF PUBLICATIONS.....		268
APPENDICES.....		269

LIST OF TABLES

		Page
Table 2.1	General properties of oxide nanotubes	36
Table 2.2	Comparison of nanotubes synthesis methods	38
Table 2.3	The development of TiO ₂ nanotubes by anodization of Ti	50
Table 2.4	Summary of work done on the anodization of Zr metal (Schmuki group)	52
Table 2.5	Summary of work done on the anodization of Zr metal (Zhao group)	53
Table 2.6	Summary of work done on the anodization of Zr metal (Skeldon group)	55
Table 2.7	Summary of work done on the anodization of Zr metal by other authors	55
Table 2.8	Summary of works on WO ₃ nanoporous applications	58
Table 3.1	Thickness and purity of metal foils used for anodization	61
Table 3.2	Chemical used for the anodization of nanotubes oxide	62
Table 3.3	Parameter of the optimized anodization in 1 M Na ₂ SO ₄ (aqueous)	68
Table 3.4	Parameter of the optimized anodization in 85% glycerol-water (organic)	68
Table 3.5	Constant parameter of anodization at different formation voltage	70
Table 3.6	Constant parameter of anodization at different time	71
Table 3.7	Constant parameter of anodization at different NH ₄ F loading	71
Table 3.8	Constant parameters of anodization at different applied voltages	72
Table 3.9	Constant parameters of anodization at different anodization time	73
Table 3.10	Constant parameters of anodization at different NH ₄ F loading	73

Table 3.11	Constant parameters of anodization at different NH_4F loading	74
Table 3.12	Variable parameters of anodization	74
Table 3.13	Constant parameters of anodization at different anodization time	75
Table 3.14	Constant parameters of anodization in different H_2O content	76
Table 3.15	Constant parameters of anodization at different anodization time	76
Table 3.16	Constant parameters of anodization at different H_2O_2 content	77
Table 3.17	Constant parameters of anodization at different anodization time	77
Table 3.18	List of ZNTs samples for photocatalytic test	78
Table 3.19	Anodization parameter for the effect of NH_4F loading	78
Table 3.20	Anodization parameters for the effect of anodization time	79
Table 4.1	samples used for photodegradation of methyl orange	112
Table 4.2	Possible surface morphologies of anodized Zr in fluoride electrolyte (listing the type of morphologies most encountered)	115
Table 4.3	Possible cross section of anodized Zr in fluoride electrolyte (listing the type of morphologies most encountered)	117
Table 4.4	Tabulated Raman peaks of ZNTs anodized at 20, 40 and 60 V	137
Table 4.5	PL band and photon energy value for sample anodized at three different voltages	140
Table 4.6	Comparison of PL band by other authors	140
Table 4.7	Average dimension of ZNTs formed at different anodization time (1 M Na_2SO_4 with 0.07 g NH_4F , at 20 V, pH 3, 1 h)	144
Table 4.8	Experimental condition to obtain nanotubes produced in aqueous electrolyte	155

Table 4.9	List of the ZrO ₂ phases based on the ICDD	168
Table 4.10	Average ZNTs dimension at different anodization time (formed in 100 ml glycerol with 0.07 g NH ₄ F at 40 V)	172
Table 4.11	ZNTs dimension at different NH ₄ F loading (100 ml glycerol at 40 V for 1 h)	174
Table 4.12	Raman peak positions attribution for the annealed ZNTs formed in 100 ml glycerol with 0.07 g NH ₄ F	179
Table 4.13	Reported Raman frequencies for ZrO ₂ modifications	179
Table 4.14	Experimental condition to obtain ZNTs formed in glycerol	180
Table 4.15	Average ZNTs dimension formed in 100 ml EG at 20 V for 1 h (different NH ₄ F loading)	185
Table 4.16	Average ZNTs dimension formed in 100 ml EG at 40 V for 1 h (different NH ₄ F loading)	188
Table 4.17	Average ZNTs dimension formed in 100 ml EG at 60 V for 1 h (different NH ₄ F loading)	191
Table 4.18	Average dimension of ZNTs dimension at different anodization time (formed in 100 ml EG with 0.3 g NH ₄ F at 40 V)	199
Table 4.19	ZNTs condition formed in EG electrolyte at different	202
Table 4.20	ZNTs dimension in different H ₂ O content (EG with 0.3 g NH ₄ F at 40 V)	207
Table 4.21	Dimension of the ZNTs at different anodization time (formed in 95 ml EG + 5 ml H ₂ O with 0.3 g NH ₄ F at 40 V)	212
Table 4.22	Dimension of ZNTs with different H ₂ O ₂ content (formed in EG with 0.3 g NH ₄ F at 40 V)	220
Table 4.23	The dimension of ZNTs at different anodization time (formed in 95 ml EG+ 5 ml H ₂ O ₂ with 0.3 g NH ₄ F at 40 V)	222
Table 4.24	Experimental condition of ZNTs produced in EG with oxidant	227

LIST OF FIGURES

		Page
Figure 1.1	Typical morphology of ZrO ₂ nanotubes showing surface and cross section morphologies	6
Figure 2.1	FESEM and TEM images showing morphologies of nanotubular anodic oxide (a) TiO ₂ (b) ZrO ₂ and (c) WO ₃	10
Figure 2.2	Schematic representation of TiO ₂ nanotubes arrays crystallization: (a) nucleation of anatase crystals (~280°C) (b) growth of the anatase crystals at elevated temperatures (c) nucleation of rutile crystals (~430°C) (d) growth of rutile crystals at higher temperatures and (e) complete transformation of crystallites in the walls to rutile at temperature above approximately 620°C (Varghese <i>et al.</i> , 2003a)	13
Figure 2.3	Morphologies which can be obtained by electrochemical anodization of metal oxide (a) a compact oxide film (b) a disordered/random nanoporous layer (c) a self-ordered nanoporous layer and (d) a self-ordered nanotubes layer	24
Figure 2.4	Flow chart of	24
Figure 2.5	Illustration of oxide growth mechanism on a metal surface	27
Figure 2.6	Schematic diagram of PDM model of reactions that occur during the formation of oxide layer. m=metal atom, M _M =metal cation in cation site, O _O =oxygen ion in anion site, V ^x _M =cation vacancy, V _O =anion vacancy, V _m =vacancy in metal phase (Macdonald, 1999).	30
Figure 2.7	Illustration of various stage of pit nucleation (Macdonald, 1999)	31
Figure 2.8	Dimensionality classification of nanostructures (Pokropivny & Skorokhod 2007)	33
Figure 2.9	A schematic summary one dimensional metal oxide nanostructures reported. (A) Nanowires and nanorods (B) core-shell structures with metallic inner core, semiconductor, or metal-oxide (C) nanotubules/nanopipes and hollow nanorods (D) heterostructures (E) nanobelts/nanoribbons (F) nanotapes (G) dendrites (H) hierarchical nanostructures (I) nanosphere assembly and (J) nanosprings (Kuchibhatla <i>et al.</i> , 2007)	35
Figure 2.10	Schematic illustration of anodization set-up forming self organized oxide	39

Figure 2.11	Illustration of the surface and side view of anodic alumina (Sulka, 2008)	40
Figure 2.12	Schematic of the kinetics of porous oxide growth on aluminium in (a) potentiostatic regimes and (b) The stages of porous structure developed are also shown (Parkhutik & Shershulsky 1992)	41
Figure 2.13	Schematic illustration of (a) oxidation region and (b) ordered porous structure	42
Figure 2.14	Typical current-time plot in electrolyte with or without fluoride ions	45
Figure 2.15	Schematic TiO ₂ nanotubes formation during anodization. (a) Morphology during phase I (b) morphology at phase II (c) morphology at phase III and (d) details of ion transport occurring in phase II and III (Macak <i>et al.</i> , 2007)	46
Figure 2.16	Illustration and SEM sequence for difference stage of TiO ₂ nanotubes formation (a) 0 min (b) 3 min (c) 10 min (d) 30 min and (e) 60 min (Macak <i>et al.</i> , 2008)	47
Figure 2.17	Schematic of surface and side view of anodic TiO ₂ nanotubes	50
Figure 3.1	Flow chart of the experimental works	61
Figure 3.2	Flow chart for procedures of experiment	63
Figure 3.3	Schematic illustration of equipments and setup in anodization process	65
Figure 3.4	Equipment set-up for photodegradation of methyl orange	67
Figure 3.5	Mechanism in Raman spectroscopy	85
Figure 4.1	FESEM images of top surface TNTs (a) Low magnification and (b) High magnification (Formed in Na ₂ SO ₄ with 0.7 g NH ₄ F, pH 3, anodization for 30 min at 20 V)	90
Figure 4.2	TNTs formed in 1M Na ₂ SO ₄ with 0.7 g NH ₄ F, pH 3, anodized for 30 min at 20 V FESEM of cross section image at (a) low magnification and (b) FESEM of cross section image high magnification (c) TEM image of tube walls and (d) EDX spectra of TNTs formed	91

Figure 4.3	FESEM images of top surface TNTs (a) Low magnification (b) High magnification and (c) Cross section (Formed in 100 ml glycerol with 0.7 g NH ₄ F, pH ~6, anodization for 30 min at 20 V)	93
Figure 4.4	Images of TNTs (a) TEM of tube cross section (b) TEM of tube top surface (c) TEM of tube bottom and (d) FESEM image of tube bottom (100 ml glycerol, 0.7 g NH ₄ F, 30 min, 20 V)	94
Figure 4.5	Illustration on the mechanism of nanotubes formation process leading to the formation of aligned nanotubes	97
Figure 4.6	Schematic illustration of the growth process of nanotubes	98
Figure 4.7	XRD patterns of TNTs (a) As-anodized and (b) Annealed for 1 h in air at different temperatures TNTs (100 ml glycerol with 0.7 g of NH ₄ F at 40 V for 30 min)	101
Figure 4.8	Raman spectra of TNTs (a) as-anodized and (b) annealed for 1 h in air (formed in 100 ml glycerol with 0.7 g of NH ₄ F at 40 V for 30 min)	103
Figure 4.9	FESEM images of annealed TNTs for 1 h in air at (a) 350°C (b) 450°C (c) 550°C and (d) 650°C (TNTs formed in 100 ml glycerol with 0.7 g of NH ₄ F at 40 V for 30 min)	105
Figure 4.10	Cross section images of annealed TNTs for 1 h in air at (a) 350°C (b) 450°C and (c) 550°C (formed in 100 ml glycerol with 0.7 g of NH ₄ F at 40 V for 30 min)	106
Figure 4.11	Illustration for the phase transformation of TiO ₂ as function of temperature	108
Figure 4.12	Schematic representation of TNTs crystallization (a) Nucleation and growth of anatase and rutile crystal at temperatures around 450°C and (b) Complete transformation of rutile at temperatures higher than 600°C	109
Figure 4.13	XRD patterns of annealed TNTs in air for 3 h (TNTs formed in 100 ml glycerol with 0.7 g of NH ₄ F at 40 V for 30 min)	110
Figure 4.14	Photodegradation of MO using anodic TiO ₂ formed in 100 ml glycerol with 0.7 g NH ₄ F electrolyte	112
Figure 4.15	Morphologies of anodic TiO ₂ (a) crystalline nanotubes structure and (b) crystalline porous structure	113

Figure 4.16	Cross sectional images of anodized Zr at (a) 10 V, (b) 20 V, (c) 40 V, (d) 50 V and (e) 60 V and (f) double layer ZNTs (1 M Na ₂ SO ₄ with 0.07 g NH ₄ F, 1 h, pH 3)	121
Figure 4.17	FESEM surface morphology of anodized Zr in 1 M Na ₂ SO ₄ with 0.07 g NH ₄ F for 1 h at (a) 10 V, (b) 20 V, (c) 40 V and (d) 50 V	123
Figure 4.18	TEM images of ZNTs anodized at 20 V in 1 M Na ₂ SO ₄ at 60 min. with 0.07 g NH ₄ F in pH 3 (a) bundled ZNTs and (b) individual ZNTs	124
Figure 4.19	EDX analysis of ZrO ₂ anodized at 20 V in 1 M Na ₂ SO ₄ at 60 min. with 0.07 g NH ₄ F in pH 3	125
Figure 4.20	Current density-time curve for anodized Zr at 20 V in 0.07 g NH ₄ F (sweep rate 1 V/s)	128
Figure 4.21	Schematic diagram of ZNTs formation (a) without dissolution of the fluoride-rich layer (b) with partial dissolution of the fluoride-rich layer (c) with total dissolution of the fluoride-rich layer and (d) double layer ZNTS	129
Figure 4.22	XRD patterns of the anodized Zr in 1 M Na ₂ SO ₄ with 0.07 g NH ₄ F, pH 3, for 1 h at different voltage (*=Zr, T=tetragonal, C=cubic, M=monoclinic)	132
Figure 4.23	Image of the ZNTs (a) ZNTs on Zr substrate and (b) ZNTs without Zr substrate	133
Figure 4.24	XRD pattern of the anodized Zr in 1M Na ₂ SO ₄ with 0.07 g NH ₄ F at 40 V without Zr substrate	133
Figure 4.25	Raman spectra of ZNTs (a) with Zr substrate anodized at 20 V, 50 V and 60 V (b) without Zr substrate anodized at 40 V (1M Na ₂ SO ₄ with 0.07 g NH ₄ F, pH 3, 1 h)	136
Figure 4.26	HRTEM of ZNTs anodized at 40 V	137
Figure 4.27	PL spectra of anodized Zr in 1M Na ₂ SO ₄ with 0.07 g NH ₄ F at 20 V, 50 V and 60 V. All samples were anodized for 1 h.	139
Figure 4.28	FESEM images of Zr anodized at 20V in 1 M Na ₂ SO ₄ with 0.07 g NH ₄ F, pH 3 at (a) 10 min, (b) 30 min, (c) 60 min and (d) 90 min	143
Figure 4.29	FESEM images of Zr anodized with different NH ₄ F loading (a) 0.01 g (b) 0.03 g (c) 0.07 g (d) 0.1 g (e) 0.3 g and (f) 0.7 g (1 M Na ₂ SO ₄ , 20 V, pH 3, 1 h)	146

Figure 4.30	XRD patterns of anodized Zr at 20 V in 1 M Na ₂ SO ₄ at 60 min with different NH ₄ F	149
Figure 4.31	XRD patterns of ZNTs (a) as-anodized and (a) annealed at three different temperatures (1 M Na ₂ SO ₄ with 0.07 g NH ₄ F at 20 V for 1 h, pH 3)	150
Figure 4.32	PL spectra of annealed ZNTs (a) annealed at 200°C (b) annealed at 400°C and (c) annealed at 600°C (anodized in 1 M Na ₂ SO ₄ at 20 V with 0.07 g NH ₄ F, 1 h, pH 3)	153
Figure 4.33	Cross section morphology of annealed ZNTs in air for 1 h (a) 200°C, (b) 400°C, and (c) 600°C (1 M Na ₂ SO ₄ at 20 V with 0.07 g NH ₄ F, 1 h, pH 3)	154
Figure 4.34	Photodegradation of methyl orange (MO) using ZNTs produced in aqueous electrolyte	156
Figure 4.35	Current-time density during anodization of Zr in glycerol with 0.07 g NH ₄ F at different voltages for 1 h	159
Figure 4.36	FESEM images of Zr anodized in glycerol with 0.07 g NH ₄ F (a) 10 V (b) 20 V (c) 30 V (d) 40 V (e) 50 V and (f) 60 V for 1 h. The images show the (i) surface view and (ii) cross section of the nanotubes formed	161
Figure 4.37	TEM images of ZNTs formed in 100 ml glycerol (a) individuals and (b) bundles	163
Figure 4.38	EDX of ZNTs formed in 100 ml glycerol with 0.07 g NH ₄ F at different voltages for 1 h	164
Figure 4.39	Schematic diagram of dissolution at tube bottom in viscous electrolyte	165
Figure 4.40	XRD patterns of Zr anodized in 100 ml glycerol with 0.07 g NH ₄ F at different voltages for 1 h	166
Figure 4.41	HRTEM images of as-anodized ZNTs formed in 100 ml glycerol with 0.07g NH ₄ F at 40 V for 1 h	168
Figure 4.42	Raman spectra of Zr anodized in 100 ml glycerol with 0.07 g NH ₄ F (a) 20V and (b) 40V for 1 h	169
Figure 4.43	FESEM images of Zr anodized in 100 ml glycerol with 0.07 g NH ₄ F at 40 V in different anodization time (a) 10 min (b) 30 min (c) 60 min and (d) 120 min. The images show the (i) surface view and (ii) cross section of the nanotubes formed	171

Figure 4.44	FESEM images of Zr anodized in 100 ml glycerol with different NH_4F loading at 40 V for 1 h: (a) 0.01 g (b) 0.07 g (c) 0.3 g and (d) 0.7 g. The images show the (i) surface view and (ii) cross section of the nanotubes	174
Figure 4.45	XRD patterns of ZNTs formed in 100 ml glycerol with different NH_4F loading at 40 V for 1 h	176
Figure 4.46	XRD patterns of ZNTs formed in 100 ml glycerol with 0.07 g NH_4F in 100 ml glycerol (annealed at different temperatures for 1 h in air)	177
Figure 4.47	Raman spectra of annealed ZNTs formed in 100 ml glycerol with 0.07 g NH_4F at 600°C	178
Figure 4.48	Photodegradation of MO using ZNTs produced in glycerol electrolyte	180
Figure 4.49	FESEM images of Zr anodized in 100 ml EG at 20 V for 1 h with different NH_4F content (a) 0.01 g (b) 0.07 g (c) 0.3 g and (d) 0.7 g	184
Figure 4.50	FESEM images of Zr anodized in 100 ml EG at 40 V for 1 h with different NH_4F content (a) 0.01 g (b) 0.07 g (c) 0.3 g and (d) 0.7 g	187
Figure 4.51	FESEM images of Zr anodized in EG at 60 V with different NH_4F loading (a) 0.01 g (b) 0.07 g (c) 0.3 g and (d) 0.7 g for 1 h	190
Figure 4.52	TEM images of ZNTs formed in EG (a) cross section view and (b) surface view	192
Figure 4.53	EDX analysis of ZNTs formed in 100 ml EG at 40 V for 1 h with 0.3 g NH_4F	192
Figure 4.54	XRD patterns of anodized Zr in 100 ml EG with different NH_4F at 40 V for 1 h	196
Figure 4.55	FESEM images of Zr anodized in EG at 40 V with 0.3 g NH_4F content (a) 5 min (b) 10 min (c) 30 min and (d) 180 min. (i) surface view and (ii) cross section of the ZNTs	197
Figure 4.56	XRD patterns of annealed ZNTs in air for 1 h at different temperatures (formed in EG with 0.3 g NH_4F , 40 V for 1 h)	199
Figure 4.57	Raman spectra of annealed ZNTs formed in 100 ml EG with 0.3 g NH_4F at 40 V (Annealing at 600°C for 1 h in air)	200

Figure 4.58	HRTEM images of anodized Zr in EG with 0.3 g NH ₄ F at 40 V for 1 h (a) as-anodized (b) and (c) annealed at 400°C for 1 h in air	201
Figure 4.59	Photodegradation of methyl orange using ZNTs formed in EG with different voltage annealed at 400°C for 1 h in air	202
Figure 4.60	FESEM images of anodized Zr in EG with 0.3 g NH ₄ F at 40 V for 1 h with H ₂ O content (a) 1 ml (b) 3 ml (c) 5 ml (d) 15 ml and (e) 30 ml (i:surface view and ii: cross section)	206
Figure 4.61	Illustration of the dissolution process at the bottom of nanotubes (a) slow etching (b) fast etching (L ₀ = initial length, L ₁ =final length)	208
Figure 4.62	XRD patterns of anodized Zr foils in EG with 0.3 g NH ₄ F at different water volume at 40 V for 1 h	209
Figure 4.63	: FESEM images of anodized Zr in 95 ml EG+5 ml H ₂ O with 0.3 g NH ₄ F at 40 V for 1 h at different anodization time (a) 10 min (b) 30 min (c) 60 min and (d) 180 min	211
Figure 4.64	XRD patterns of anodized Zr foils in 95 ml EG+5 ml H ₂ O with 0.3 g NH ₄ F at different anodizing time at 40 V	212
Figure 4.65	TEM images of anodized Zr in 95 ml EG+ 5 ml H ₂ O with 0.3 g NH ₄ F at 40 V for 1 h (a) cross section nanotubes and (b) top view	213
Figure 4.66	HRTEM showing images of anodized Zr in 95 ml EG+ 5 ml H ₂ O with 0.3 g NH ₄ F at 40 V for 1 h with H ₂ O (a) low magnification lattice fringes (b) high magnification lattice fringes and (c) SAED pattern	214
Figure 4.67	XRD patterns of anodized Zr foils in 95 ml EG+5 ml H ₂ O with 0.3 g NH ₄ F at 40 V annealed in different temperature	215
Figure 4.68	Raman spectra of anodized Zr foils in 95 ml EG+5 ml H ₂ O with 0.3 g NH ₄ F at 40 V annealing at 600°C	216
Figure 4.69	FESEM images of anodized Zr in EG with 0.3 g NH ₄ F at 40 V for 1 h in different H ₂ O ₂ content (a) 1 ml (b) 3 ml and (c) 5 ml	219
Figure 4.70	FESEM images of anodized Zr in 95 ml EG+5 ml H ₂ O ₂ with 0.3 g NH ₄ F at 40 V for different time (a) 1 min (b) 15 min and (c) 30 min	221
Figure 4.71	TEM images of anodized Zr in 95 ml EG+5 ml H ₂ O ₂ with 0.3 g NH ₄ F at 40 V (a) Cross section nanotubes (b) Top view (c)	223

	Cross section of tube wall (high magnification) and (d) bottom view	
Figure 4.72	EFTEM images of anodized Zr in 95 ml EG+ 5 ml H ₂ O ₂ with 0.3 g NH ₄ F at 40 V (a) Overall tube length (b) TEM of ZNTs tube wall (c) Oxygen mapping and (d) Zr mapping	224
Figure 4.73	XRD patterns of ZNTs samples formed in 95 ml EG+ 5 ml H ₂ O ₂ annealed at 200 °C, 400 °C and 600 °C	225
Figure 4.74	Photodegradation of MO using ZNTs formed in EG with oxidation agent	227
Figure 4.75	FESEM images of anodized W in glycerol electrolyte with 0.3 g NH ₄ F at 40 V for 1 h	228
Figure 4.76	FESEM images of anodized W in electrolyte with different NH ₄ F loading (a) 0.07 g (b) 0.1 g (c) 0.3 g and (d) 0.7 g (1 M Na ₂ SO ₄ at 40 V with 0.3 g NH ₄ F for 1 h, pH 3)	230
Figure 4.77	XRD patterns of anodized W in 100 ml Na ₂ SO ₄ , pH 3 at 40 V for 1 h in different NH ₄ F loading (a) as-anodized and (b) annealed at 500 °C for 1 h in air	231
Figure 4.78	Schematic illustration for the mechanism of segmented WO ₃ nanotubes	234
Figure 4.79	Current density versus time curves recorded during anodization of W for the formation of segmented WO ₃ (in 1M Na ₂ SO ₄ at 40 V with 0.3 g NH ₄ F for 1 h)	235
Figure 4.80	FESEM images of anodized W in electrolyte with different pH (a) pH~3 and (b) pH~6 (samples were anodized in 1M Na ₂ SO ₄ at 40 V with 0.3 g NH ₄ F for 1 h)	236
Figure 4.81	XRD patterns of anodized W at pH 3 and 6 (annealing was done at 500 °C for 1 h in air)	238
Figure 4.82	Raman spectra of as-anodized and annealed (500 °C, 1 h in air) WO ₃ samples made in 1 M Na ₂ SO ₄ at 40 V with 0.3 g NH ₄ F, pH 3 for 1 h	239
Figure 4.83	PL spectra of WO ₃ samples made in 1M Na ₂ SO ₄ at 40 V with 0.3 g NH ₄ F, pH 3 for 1 h (a) as-anodized and (b) annealed (500 °C, 1 h in air)	240
Figure 4.84	FESEM images of anodized W in electrolyte with different time (a) 30 min (b) 60 min and (c) 120 min (1M Na ₂ SO ₄ at 40 V with	242

0.3 g NH₄F)

Figure 4.85	XRD patterns of anodized W at different anodizing time	243
Figure 4.86	TEM images of WO ₃ (a) surface and (b) cross section (1M Na ₂ SO ₄ , 0.3 g NH ₄ F at pH 3 for 1 h)	244
Figure 4.87	Photodegradation of MO using WO ₃ nanotubes produced in 1M Na ₂ SO ₂ with 0.3 g NH ₄ F, pH 3 at 40 V	245

LIST OF ABBREVIATIONS

ZNTs	Zirconium oxide nanotubes
TNTs	Titanium oxide nanotubes
WNTs	Tungsten oxide nanotubes
C	Cubic
T	Tetragonal
M	Monoclinic
MO	Methyl orange
PC	Photocatalytic
SEM	Scanning Electron Microscopy
FESEM	Field Emission Scanning Electron Microscopy
XRD	X-ray Diffraction
TEM	Transmission Electron Microscopy
HRTEM	High Resolution Transmission Electron Microscopy
PL	Photoluminescence
EFTEM	Energy Filtered Transmission Electron Microscopy

LIST OF SYMBOLS

%	Percentage
<	Less than
>	More than
°C	Degree Celsius
°C/min	Degree Celsius per minute
cm	Centimetre
h	Hour
L	Liter
m	Meter
min	Minute
ml	Milliliter
mm	Millimeter
wt %	Weight percent
A	Ampere
V	Voltage
nm	Nanometer
g	Gram
s	Second
d	Thickness
eV	Electron volt
λ	Wave length
T	Temperature

PEMBENTUKAN OKSIDA TIUB NANO MELALUI KAEDAH PENGANODAN LOGAM “VALVE”

ABSTRAK

Penghasilan tiubnano TiO_2 (TNTs), tiubnano ZrO_2 (ZNTs) dan tiubnano bersegi WO_3 (WNTs) melalui penganodan logam-logam Ti, Zr dan W telah berjaya dibentuk di dalam elektrolit akueus dan organik yang berflorin. Bagi elektrolit akueus, 1 M Na_2SO_4 (pH 3). Gliserol dan glikol etilena yang mempunyai pH neutral telah diguna sebagai elektrolit organik. Morfologi dan struktur bagi tiub nano beroksida yang terbentuk telah dikaji. Melalui penganodan, faktor-faktor utama yang mempengaruhi struktur tiub nano adalah jenis-jenis elektrolit, komposisi elektrolit, voltan penganodan yang dikenakan pada anod dan masa penganodan. Didapati TNTs dan ZNTs boleh dibentuk di dalam elektrolit akueus dan organik. Walau bagaimanapun, WNTs hanya boleh dibentuk di dalam elektrolit akueus. Morfologinya bukanlah tiub nano tetapi merupakan tiub nano bersegi. Kedua-dua ZNTs dan TNTs adalah sangat tersusun, selaras dengan baik dan tumbuh secara menegak terhadap kerajang logam. TNTs yang terbentuk, mempunyai diameter purata berjulat 50-100 nm dan panjang sekitar 700 nm. Analisa terperinci terhadap TNTs selepas sepuhlindap menunjukkan pembentukan fasa berlaku pada suhu 350 pada 450°C transformasi telah berlaku. Fasa rutil mendominasi pada suhu >600°C. Mekanisma pembentukan ZNTs telah dicadangkan di sini berdasarkan tiga proses utama pada peringkat awal penganodan; pembentukan ZrO_2 beranodik, pembentukan liang, pembentukan lubang diikuti dengan proses pemisahan lubang pada tiub nano dalam keadaan seimbang. Morfologi ZNTs seterusnya boleh diklasifikasikan sebagai lapisan berkembar, lapisan tunggal, berkumpul dan mendakan di atas ZNTs.

Morfologi tersebut telah dibincangkan di dalam kajian ini. Di samping itu, penganodan ZNTs yang terbentuk di dalam elektrolit berakueus adalah sangat berhablur dengan modifikasi tetragonal/kubik tetapi kurang berhablur di dalam elektrolit berorganik. Penambahan agen pengoksidaan (H_2O dan H_2O_2) di dalam elektrolit glikol etilena telah meningkatkan kadar pembentukan ZNTs. Di dalam glikol etilena dengan elektrolit H_2O_2 kadar pembentukan ialah sebanyak 296.4 nm/min (berbanding dalam etilena glikol tanpa agent pengosidaan: 200 nm/min). WNTs adalah amorfus dan sepuhlindap pada suhu $400^\circ C$ selama 1 h mengubah amorfus WO_3 kepada berhablur monoklinik. Pembentukan WNTs agak berbeza dari ZNTs dan TNTs disebabkan oleh pembentukan semula oksida di kawasan antara tiub dan juga di dalam tiub tersebut. Sifat photoluminasi dan fotopemangkinan oksida ini juga telah di kaji.

FORMATION OF NANOTUBULAR OXIDE BY ANODIZATION OF VALVE METALS

ABSTRACT

The formation of TiO₂ nanotubes (TNTs), ZrO₂ nanotubes (ZNTs) and segmented WO₃ nanotubes (WNTs) by anodization of Ti, Zr, and W metal was successful in fluorinated aqueous and organic electrolyte. In aqueous electrolyte, acidic 1 M Na₂SO₄ (pH 3). Glycerol and ethylene glycol were the organic electrolyte with their neutral pH. The properties including morphology and structural of the nanotubular oxide formed were investigated. During anodization, the main factors effecting nanotubular structures are types of electrolyte, its composition, anodization voltage applied to anode and anodization time. It was found that TNTs and ZNTs can be formed in both aqueous and organic electrolytes. However WNTs can only be formed in aqueous electrolyte. The morphology of WNTs also different such that they are not really nanotubular but in a form of segmented porous structure. Both ZNTs and TNTs are highly ordered, well aligned and grow perpendicular to the metal foil. The TNTs formed, had the average diameter ranging from 50-100 nm and length of 700 nm. Detailed analysis of annealing on TNTs reveals that, phase formation to anatase occurred at 350°C at 450°C transformation happened. At temperature > 600°C rutile phase dominated. The mechanism of ZNTs formation is found to be based on three dominating process at the early stage of anodization; anodic ZrO₂ formation, pits formation, pore formation followed by pore separation process to form nanotubes. The morphologies of ZNTs can be further classified as double layer, single layer, bundled and precipitates on ZNTs. The origin of these morphologies is discussed in this thesis. As-anodized ZNTs, formed in aqueous

electrolyte is highly crystalline with tetragonal/cubic modification. In organic electrolyte, the crystallinity seems poorer. The addition of oxidants (H_2O and H_2O_2) in ethylene glycol electrolyte increased the rate of ZNTs formation. In ethylene glycol with H_2O_2 the rate of formation is 296.4 nm/min (compared to 200nm/min in ethylene glycol without oxidant). WNTs are amorphous and annealing at 400°C for 1 h transformed the amorphous to crystalline of monoclinic WO_3 . The formation mechanism of WO_3 is different from ZNTs and TNTs since regeneration of oxide occurs in between tubes as well as within tubes. The photoluminescence and photocatalyst properties of these oxides were also investigated.

CHAPTER 1

INTRODUCTION

1.1 Background

Nanostructures are structures with at least one dimension in the range of 1-100 nm. These structures have attracted increasing interest due to their fascinating unique characteristics allowing applications in various industries. The ability to produce materials with small structures (in nanoscale) has been seen as one of the most important aspect in modern science and technology. Once synthesized, there are large numbers of opportunities that these so-called nanomaterials can offer.

Nanotubular materials as the subset of nanomaterials and their surface, structural and other properties highlight many important uses in various fields. Nanotubes of both organic and inorganic have been used for many applications in electronic industries, for energy generation and energy saving technologies, as catalysts, catalysts support, in sensor technology, in biomedical applications, as membrane, as absorbent materials and in purifications of contaminated water and air (Kumara *et al.*, 2007). Nanotubes are typical examples of the so-called 1 dimensional (1D) nanostructures. The diameter of 1D nanomaterials has to be < 100 nm but the length can be > 100 nm. The length-to-diameter ratio (aspect ratio) is therefore can be significantly greater than unity (Spanier 2006). Research and development on the synthesis and applications of inorganic nanotubes especially oxide nanotubes have attracted much attention. This is because oxide nanotubes can be used in various applications, and the structure can be easily formed. Typically the formation of nanotubes can be produced by template based, hydrothermal and sol-gel method. The formation of self-ordering growth nanotubes by anodic oxidation has gained wide interest. This process resemble the example of electrochemical self-ordering which

was successfully done in forming ordered porous Al_2O_3 by anodization of Al. In this research, nanotubular ZrO_2 , TiO_2 and WO_3 were synthesized by anodic process on large area substrate making a three dimensional (3-D) network of aligned nanotubes film. These oxides are functional oxides with many desirable characteristics which allow them to be used in green technology. The thesis is focused mainly on optimizing anodic oxidation process for the formation of these oxides in nanotubular form and also on exploring some of the properties of the nanomaterials to be applied in green technology.

Anodic oxidation is an electrochemical process to make thin oxide film on a metallic substrate. Two types of oxide layer can be formed by anodic process: compact and porous. Porous layer can be further classified as random porous and ordered porous. Ordered porous can either be in a form of connected pores or as nanotubular whereby the dissolving pore boundaries will formed discreet nanotubular structure. The formation of pores is by the porosification process of barrier oxide. Fluoride is needed for this porosification to occur. In considering structure growth of anodic oxide with nanotubular structure, Ghicov & Schmuki (2009) had produced a comprehensive review on how nanotubes form. The review is however emphasizing on TiO_2 nanotubes formation. Meanwhile applications of the TiO_2 nanotubes have been reviewed by Grimes & Mor (2009).

As mentioned electrochemical anodization would form oxide film. In this present work, Ti was anodized to form TiO_2 , Zr forming ZrO_2 and W forming WO_3 films. These oxides have many applications and many features of these oxide become of practical value if they are made in thin film form. When the film experienced porosification with continual pore boundaries dissolution, film will finally comprises of ordered nanotubular structure. Finally a 3-D network is said to

form. This structure has many advantages and applicable for solar cell, photoelectrochemical and photocatalysis.

One interesting example is as photocatalyst. The nanosized structures of photocatalyst influence the specific surface area for reaction site. Hence, the use of nanotubular photocatalyst can create relatively large specific surface area thus more reactions can happen. Besides that, the thin tube wall can also increase the photocatalytic ability due to short distance of the excited electron and holes to travel to the surface, thereby reducing the probability of electron-hole recombination. The thin wall enables efficient charge transfer of photo-excited electrons and holes to the surface active sites. In addition by using anodic film as photocatalyst it is recyclable and can be reused as it is supported. The nanotubular supported film photocatalyst can overcome the problems encounter by nanoparticles photocatalyst such as TiO_2 . Whereby, using TiO_2 nanoparticles, the aggregation of particles in suspension cause rapid loss in active sites and photocatalytic efficiency. The post separation that needs to be done on the photocatalytic system could be tedious and unpractical which consume more energy and time.

1.2 Problem statement

The synthesis of TiO_2 nanotube arrays by anodization of Ti foil in the presence of fluorine ions have been vastly reported with two leading works reported by Roy *et al.*,(2011) and Rani *et al.*,(2010). The as-anodized TiO_2 nanotubes are amorphous. For many applications crystallinity is desired. TiO_2 comes in anatase (450°C) and rutile (600°C). For example, anatase is preferred in photocatalysis and catalysis whereas rutile is mostly used in gas sensors and dielectrics. However to the best of our knowledge no systematic study has been made to understand the crystallinity

formation of TiO₂ nanotubes apart from the works of Varghese *et al.*, (2003a) and Yang *et al.*, (2008). The crystallinity of TiO₂ nanotubes actually varies with synthesis technique. For anodic TiO₂ it is important to examine the crystallization and phase transition of TiO₂ nanotubes when the nanotubes are subjected to heat treatment. Another important aspect is on the stability of nanotubes at high temperature. It is known that, nanoscale materials have high surface energy and with additional energy from the heating process, the materials can get sintered. This would destroy the nanotubular structure as the tube will get sintered and merged together. Structural stability of the TiO₂ nanotubes at elevated temperature is important for their application and this need to be examined during the process of crystallization at elevated temperature. In this thesis the effect of temperature on phase transition of TiO₂ nanotubes prepared by anodization of Ti in fluoride electrolyte as well as the stability of the nanotubular architecture of TiO₂ nanotubes arrays at elevated temperature is investigated.

ZrO₂ on the other hand, is a unique ceramic oxide. ZrO₂ can be formed in nanotubular form typically by template based, hydrothermal and sol gel method. This thesis is looking at the formation ZrO₂ nanotubes by anodic process. Similar procedure was adopted to form ZrO₂ nanotubes as that to TiO₂ nanotubes. Due to the immaturity of ZrO₂ nanotubes research, only a few groups are working on this material. Skeldon group's and Schmuki group's are the researchers who progressively reported on the formation of ZrO₂ nanotubes by anodic oxidation. There are limited of data on the ZrO₂ nanotubes properties available as not many works was reported on ZrO₂ nanotubes. As will be explained further in this thesis, ZrO₂ comes in three polymorphs, cubic, tetragonal and monoclinic. Whilst the cubic and tetragonal are high temperature phases, monoclinic is the room temperature

stable form of ZrO_2 . However, doping of the oxide can be done to stabilize both tetragonal and cubic at room temperature. The question on what exactly the energy band gap of doped ZrO_2 in cubic and tetragonal form has been aroused for decades now. Theoretical calculation for example by Chang and Doong (2007) pointed out that the band gap of monoclinic, tetragonal and cubic are in the range of 3.12-5.42, 4.10-13.33 and 3.25-12.3 eV respectively. There is lack of information available on the luminescence properties of ZrO_2 nanotubes especially those made by anodization process. The difficulty for obtaining pure ZrO_2 phase without any doping has resulted in no accurate information for luminescence and as well as the band gap of this material. However using anodization, high stabilized phase was produced without having any foreign dopants and it is of interest to study the luminescent of the stabilized ZrO_2 . Moreover the nanotubular architecture has made it more interestingly to be investigated. To date there is no works on the measured bandgap of pure ZrO_2 cubic or tetragonal in nanotubes form. In this work, we attempted on performing photoluminescence studied.

The use of anodization process is unique since it can form a high temperature stable cubic or tetragonal ZrO_2 phase as reported by Habazaki *et al.*, (2000). The existence of cubic or tetragonal ZrO_2 by anodic was found to be dependent on anodization condition. Here, a thorough study was done to produce the optimum ZrO_2 nanotubes structures. Two electrolytes were used: organic and aqueous added with fluoride. This thesis looks at the morphology of ZrO_2 nanotubes formed in both electrolytes. For anodization in organic electrolyte, contribution of oxidant needs to be considered. The lack of oxidant hinders the growth of ZrO_2 nanotubes. So, we have attempted to test the presence of water and hydrogen peroxide as the oxidizing

agent to enhance the growth of ZrO_2 . The morphology of ZrO_2 nanotubes produced by anodization is shown in Figure 1.1.

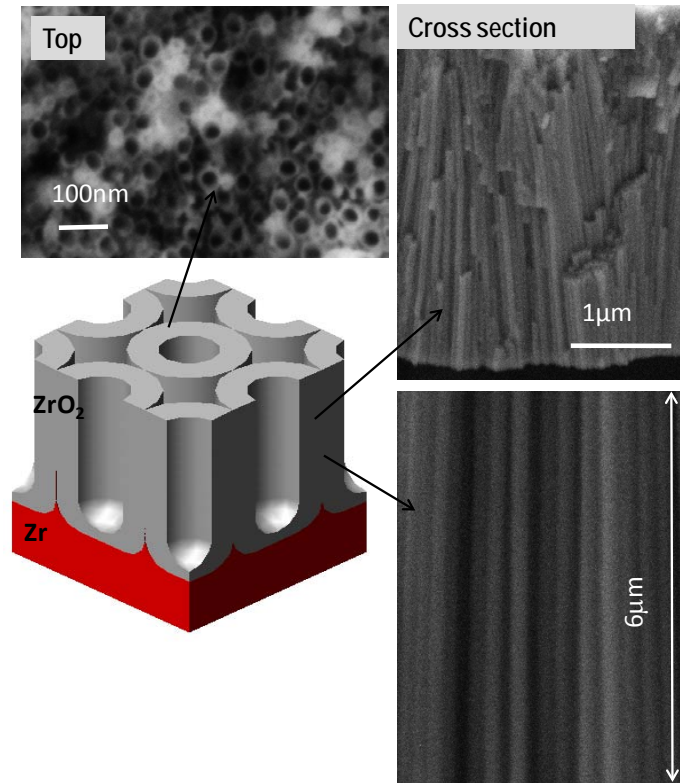


Figure 1.1: Typical morphology of ZrO_2 nanotubes showing surface and cross section morphologies

Works on photocatalytic properties of ZrO_2 have been reported by Alvarez *et al.*, (2007), Botta *et al.*, (1999) and Karunakaran & Senthilvelan (2005). From these works ZrO_2 is said to be a potential photocatalyst and exhibit a high activity. This characteristic of ZrO_2 arises from its highly negative flat-band potential and wide band gap (Sayama & Arakawa 1996). There is no reported work on the photocatalytic properties of the ZrO_2 nanotubular structures. The use of nanotubular structure would provide larger surface area. Furthermore, thin film containing nanotubes would be a better option as opposed to suspension of particles in solution.

WO₃ is an indirect bandgap semiconductor (Feng *et al.*, 2005) which has been extensively studied due to their application in electrochromic (Nah *et al.*, 2008), photocatalytic (Baeck *et al.*, 2003) and gas sensors (Li *et al.*, 2004). The photoelectrochemical properties of WO₃ have made it possible for these applications. Due to broad application of WO₃, the formation of porous WO₃ with high surface area has drawn great interest. The preparation of porous WO₃ by anodization was first reported by Mukherjee *et al.*, (2003) by galvanostatic anodization. Then, nanoporous WO₃ by anodization of W was reported by Berger *et al.*, (2006). However, none of these works reported neither on the detailed mechanism of nanoporous oxide formation nor the exact feature of the oxide.

In this thesis WO₃ was made in 3-D network on W foil. As to date, there are not many available reports on the formation of WO₃ nanotubes. The most comprehensive study has however been done by Kalantar-zadeh *et al.*, (2009) and Watcharenwong *et al.*, (2008). WO₃ nanotubes were then used as photocatalyst and their properties were evaluated. WO₃ has a narrow band gap (2-2.8 eV) and hence can absorb visible light up to 500 nm. This makes WO₃ attractive for the use of a photocatalyst (Kou *et al.*, 2010) under visible light.

1.3 Research objectives

The main aim of this work is to form the nanotubular oxide and following are the list of objectives for this research:

- (1) To study the morphology of nanotubular TiO₂ formed by anodization of Ti in fluoride electrolyte and the effect of heat treatment on the phase formation and transformation of TiO₂.

- (2) To investigate the morphology and characteristic (structural, luminescence and crystallinity) of the nanotubular ZrO_2 and WO_3 formed by anodization on Zr foil, in fluoride electrolytes.
- (3) To proposed appropriate mechanism and to compare the properties and mechanistic growth of the oxides (TiO_2 , ZrO_2 and WO_3) formed by anodization.

1.4 Thesis outline

This project was conducted to form the 3-D network of TiO_2 , ZrO_2 and WO_3 in the form of nanotubular structure. First, anodization process was performed in organic and aqueous bath containing NH_4F to form the nanotubes. The photocatalytic ability of the formed oxides was then tested using methyl orange dye as the indicator by using UV light irradiation. This is to evaluate the ability of the produced nanostructures oxide as the photocatalyst.

Chapter 1 is the overall introduction for the whole thesis. A brief introduction on the nanostructured materials and anodization process is in chapter 2, as well as the mechanism to form one dimensional (1-D) nanotubular metal oxide. The applications of the nanotubular oxide are presented in this part. Chapter 3 is on methods of experimental works for this research. Chapter 4 is the results and discussion for anodization of ZrO_2 , TiO_2 and WO_3 nanotubes as well as the photocatalytic application of the produced oxides. Chapter 5 is on the conclusion and suggestions for further studies on this work.

CHAPTER 2

LITERATURE REVIEW

2.1 Introduction

This chapter reviews important topics related to this thesis. As several metal foils (valve metal) were anodized for nanotubular oxide formation, the subject of anodic process and nanotubes formation are reviewed in here. Literature survey on the characteristics and applications of the nanotubes formed are presented as well focusing on the structural, optical, morphological and photocatalytic properties of anodic TiO₂, ZrO₂ and WO₃.

2.2 Valve metal oxide

Metals such as Ti, W, Zr, Hf, Ta and Nb belong to a class of so-called valve metals. It is possible to grow anodic oxide on valve metals with considerable thickness in aqueous electrolyte by anodic oxidation. Valve metals are mainly transition group metals. Transition metals are element whose atom has an incomplete d sub-shell, or which can give rise to cations with an incomplete d sub-shell (Cox 2010). Oxides grown on transition metals are transition metal oxides (valve metal oxide) and it is well known that transition metal oxides have many interesting properties as shall be discussed in the next sub heading.

2.2.1 Properties of transition (valve) metal oxide

TiO₂, ZrO₂ and WO₃ are transition metal oxides. TiO₂ occurs as a mineral in the nature while pure mineral of ZrO₂ is rare in nature and most of Zr occurs as zirconium silicate (ZrSiO₄). Tungsten is found in nature only combined in chemical compounds. WO₃ is obtained as intermediate in the recovery of W from its minerals.

Many features of these valve metal oxides become useful and feasible if the material is in micro-or nanostructures specifically they exhibit a high surface area.

Various research works are now focusing on the design and controlled thin film of transition metal oxides formation with nanostructures via innovative synthesis strategies. The nanostructured film of oxides can be synthesized by chemical approaches; the most typical ways are sol-gel and hydrothermal approaches or physical processes: vapor processes. The morphologies that can be produced include nanofilms or films with nanostructures: nanowires, nanorods and nanotubes or films comprising of nanocrystallites.

Electrochemical process through anodic oxidation offers the formation of film comprising of aligned, ordered nanotubes covering the surface of metal foil homogeneously. Therefore regardless of the size of the metal foil, such 3-D network of nanotubes can be fabricated on the surface of the metal. Nonetheless, there are various parameters ought to be optimized in order to produce nanotubes with uniform diameter, that can cover the whole area of the metal foil uniformly and with the same length throughout. In this work, anodization parameters were studied. Typical nanotubular structures formed by anodic oxidation of Ti, W, and Zr derived from this research are shown in Figure 2.1 (a), (b) and (c) respectively.

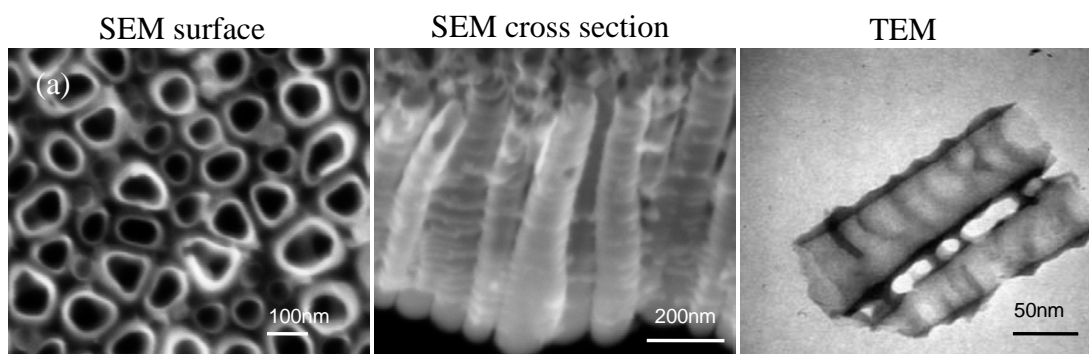


Figure 2.1: FESEM and TEM images showing morphologies of nanotubular anodic oxide (a) TiO_2 (b) ZrO_2 and (c) WO_3

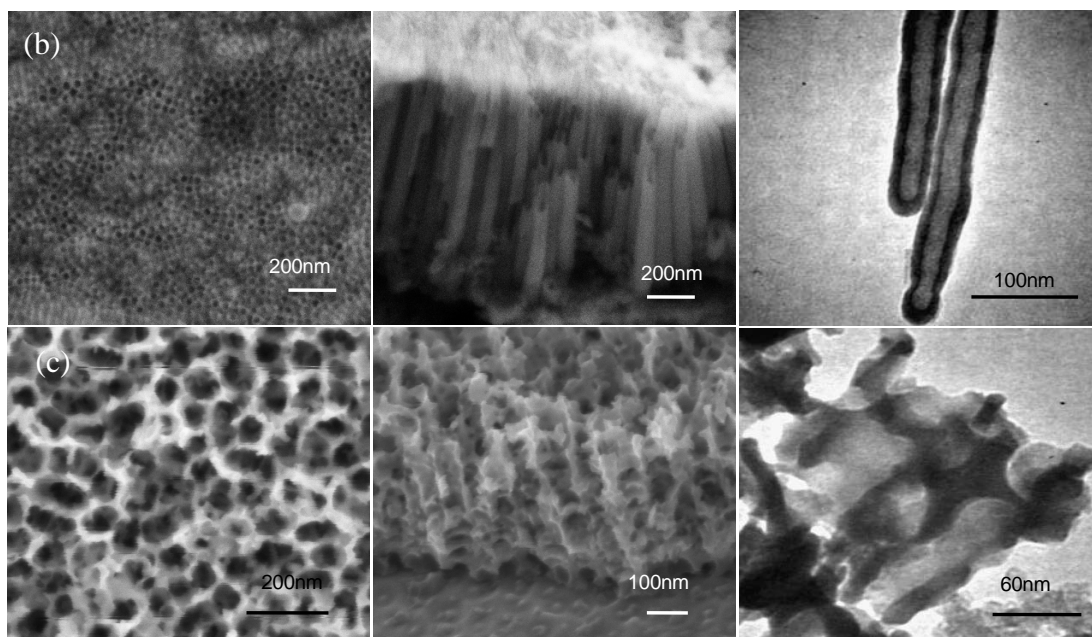


Figure 2.1: FESEM and TEM images showing morphologies of nanotubular anodic oxide (a) TiO_2 (b) ZrO_2 and (c) WO_3 (continued)

Having these structures in mind, this chapter will review some of the properties of these oxides, how these structures are formed, and what the applications of these structures are. More importantly as mentioned, anodization parameters are the key factors that allow the formation of this oxide. Therefore, works done by other researchers on the topic of nanotubes formation by anodization is reviewed here thoroughly. The introduction for these oxides will however be given first.

2.2.1.1 Properties of TiO_2

TiO_2 is a multi-functional oxide that obviously has numerous interesting applications. TiO_2 is an inert material; biologically and chemically therefore it provides a good condition to be used especially in medical application (Brammer *et al.*, 2008). It is a harmless material to human and chemically stable with respect to chemical corrosion. Thus it is widely used for orthopedic or dental implants.

Porous TiO₂ films can be used as electrode in dye sensitized solar cell (DSSC) (Zukalova *et al.*, 2005) and as electrode in photoelectrochemical cells (PEC) (Fujishima & Honda 1972). It is also a very well known oxide exhibiting photocatalytic property (Fujishima & Honda 1972) and also self-cleaning property (Roméas *et al.*, 1999).

TiO₂ nanotubes formed by anodization are normally amorphous. But the polymorph of TiO₂ exists in the form of anatase and rutile depending on the temperature and pressure at which the material is exposed to. TiO₂ normally undergoes anatase to rutile phase transformation when the temperature is raised at least above 450°C (Tang *et al.*, 2003). Anatase stabilization depends on synthesis conditions, but rutile can only be obtained at high temperature (Bokhimi *et al.*, 2001). For the case of phase transformation in TiO₂ nanotubes, Varghese *et al.*, (2003a) has suggested a model to explain the crystallization of amorphous TiO₂ nanotubes as schematically shown in Figure 2.2. They reported that the nucleation of anatase phase occur at temperatures between 230 and 280°C, Figure 2.2 (a). These crystallites grow in size with increasing temperature as shown in Figure 2.2 (b). As the crystallites grow some of the closely spaced crystallites coalesce to form larger crystallites while others establish grain boundary contacts. The size of the crystallites in the walls is restricted due to the constraints imposed by the walls. At temperatures around 430°C, rutile formation occurs specifically at the nanotubes Ti support interface region (Figure 2.2(c)) leaving the anatase crystallite in the walls unaffected. As the annealing was done at higher temperature between 480 and 580°C, both Ti and larger anatase crystals at the interface can be directly transformed into rutile. Smaller anatase crystallites grow at higher temperatures (~ 620°C), yielding a larger anatase grain size. Eventually, the anatase crystallites in the walls are consumed by

the developing rutile layer (Figure 2.2 (d)). Hence, a complete rutile phase can be seen for sample annealed at 680°C (Figure 2.2 (e)).

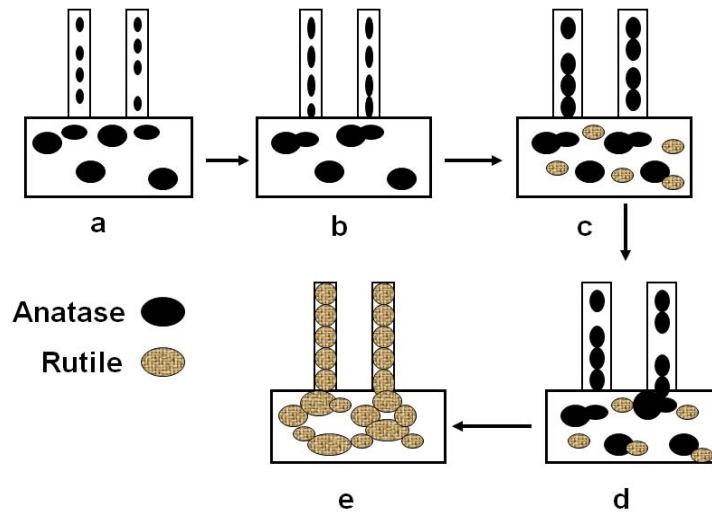


Figure 2.2: Schematic representation of TiO₂ nanotubes arrays crystallization: (a) nucleation of anatase crystals (~280°C) (b) growth of the anatase crystals at elevated temperatures (c) nucleation of rutile crystals (~430°C) (d) growth of rutile crystals at higher temperatures and (e) complete transformation of crystallites in the walls to rutile at temperature above approximately 620°C (Varghese *et al.*, 2003a)

Generally, crystallization or phase transformations take place through nucleation and growth processes (Kondo & Domen 2007). The mechanism of phase transformation in TiO₂ from anatase to rutile has been studied especially for particles of TiO₂. The process involves breaking two of the six Ti–O bonds to form new bonds with the transformation activation energy calculated to be (264 kJ/mol) for the oxygen annealed samples (Navrotsky & Kleppa 1967; Shannon & Pask 2006). The nucleation and growth of rutile from anatase can occur through different processes. Zhang & Banfield (2000) reported that the nucleation can take place (i) at the interface of two contacting anatase particles which results in transforming the anatase grains into rutile grain and (ii) in the bulk or on the surface of a large anatase grain. During the nucleation process of rutile, the crystallites may rotate and reorient if

sufficient volume is available (Gouma & Mills 2004). So if the volume is not sufficient, as in the case of nanoparticles with diameter < 14 nm then, transformation will not happen (Zhang & Banfield 2000). It is also anticipated that anatase to rutile transformation may not happen in nanotubes with wall < 14 nm. The growth of rutile occurs when (i) a rutile crystallite comes into contact with an anatase crystallite consuming it to form a larger rutile crystallite; or (ii) two rutile nuclei (or crystal) merging together (Zhang & Banfield 2000). In the case of temperature annealing of TiO₂ nanotubes supported on Ti, as discussed by Varghese, the formation of rutile is also possible when Ti support is oxidized forming rutile crystals. The growth of these crystals will eventually thicken the wall of the nanotubes eventually destroying the nanotubular structure.

The formation of crystalline TiO₂ is important for both TiO₂ in powdered form or nanotubes especially when the oxide is to be used as catalyst or photocatalyst and in solar energy generation devices like solar cell. Obviously the crystallinity of TiO₂ affects its electronic properties. The crystallinity of TiO₂ can be investigated by XRD and Raman spectroscopy. Frequently (011) anatase and (110) rutile co-exist in nanostructured TiO₂ as often shown from XRD pattern of TiO₂. Raman spectroscopy can also be used to further investigate the crystallinity of nanostructured TiO₂. According to Qian *et al.*, (2005) there are 6 Raman active modes for anatase; A_{1g} + 2B_{1g} + 3E_{1g} which can be identified at 144 cm⁻¹(E_g), 197 cm⁻¹ (E_g), 399 cm⁻¹ (B_{1g}), 513 cm⁻¹ (A_{1g}), 519 cm⁻¹ (B_{1g}) and 639 cm⁻¹ (E_g). Rutile TiO₂ on the other hand have four Raman active modes; A_{1g}, B_{1g}, B_{2g}, and E_g at 143, 447, 612 and 825 cm⁻¹ respectively.

The photocatalysis degradation of various organic systems on irradiated TiO₂ is well documented in literature (Aguedach *et al.*, 2005; Khataee *et al.*, 2010) and

indeed has been related to the percentage of anatase and rutile phases within the oxide. Photocatalysts TiO_2 can be activated by irradiating the oxide with appropriate light and due to this; excitation of electrons from the valance band of the oxide can happen leaving holes in the conduction band. The generation of electron and hole pair leading to the formation of hydroxyl radical ($\bullet\text{OH}$) and superoxide radical ($\text{O}_2^{\bullet-}$) ions. These radicals are the primary oxidizing species in the photocatalytic oxidation process or termed Advance Oxidation Process (AOP). The mechanism for the process is shown by Fujishima *et al.*, (2000). The oxidative reactions would result in the degradation of the pollutant and the efficiency of the degradation will depend upon the oxygen concentration, which determines the efficiency with which the conduction band electrons are scavenged and the electron-hole recombination is prevented. TiO_2 is obviously an important material for the degradation of various pollutants hence can be used in waste treatment process for instance.

TiO_2 is also an anti-bacteria material which is known to be a good material in killing bacteria like E. Coli strains which can be obtained from soil and sewage samples. In the event of nanotechnology, TiO_2 in nanotubular structures have been experimented as photocatalyst material in degradation of organic compounds such as dyes and phenolic as well as anti-microbial in treating water.

Typically in the experiment to investigate the photocatalytic properties of TiO_2 , the nanotubes structures was formed by anodic oxidation of Ti forming ordered and align nanotubes then the nanotubes will be placed in a reactor containing known amount and concentration of methyl orange or other dye. The decomposition of the dye will be investigated by UV-Vis spectroscopy.

The formation of pure anatase and rutile or a mixture of anatase and rutile TiO_2 is important because the photocatalytic ability of TiO_2 is depended on its

modification. Anatase TiO_2 have a band gap of 3.2 eV, corresponding to UV wavelength of 385 nm. Pure anatase exhibits lower rates of recombination of electron and holes in the oxide in comparison to rutile due to its 10-fold greater rate of hole trapping (Riegel & Bolton 1995). Rutile has a smaller band gap of 3.0 eV with excitation wavelengths that extend into the visible at 410 nm. The efficiency of most photocatalysts is determined to a large degree by recombination rates. Despite the fact that the photoactivity of rutile extends into the visible light range, pure phase rutile is photocatalytically inactive. It has been established that rutile exhibits high rates of recombination in comparison to anatase (Hurum *et al.*, 2005). Moreover the adsorptive affinity of anatase for organic compounds is higher than that of rutile (Stafford *et al.*, 1993).

In rutile and anatase TiO_2 , the position of the valence band is deep, and the resulting positive holes show sufficient oxidative power. However, the conduction band is positioned near the oxidation-reduction potential of the hydrogen, indicating that both types are relatively weak in terms of reducing power. It is known that the conduction band in the anatase type is closer to the negative position than in the rutile type. Therefore, the reducing power of the anatase type is stronger than that of the rutile type. Due to the difference in the position of the conduction band, the anatase type exhibits higher overall photocatalytic activity than the rutile type. This is also supported by several authors whereby they agreed that anatase is better for this application (Hirakawa *et al.*, 2007; Malinger *et al.*, 2011).

2.2.1.2 Properties of ZrO_2

Zirconium dioxide (ZrO_2) is a technologically important material that can be used not only in structural ceramics but also in advanced application. For instance

ZrO₂ has been used as catalyst and catalyst support because of its good physicochemical properties, surface acidity and reactivity (Yamaguchi 1994). ZrO₂ is also known to have high ionic conductivity hence is useful as oxygen conductor. It has been used in solid oxide fuel cell and as oxygen sensor (Tan & Wu 1998). It is also stable under a reducing atmosphere and photo irradiation. These properties make ZrO₂ the most suitable candidate as a refractory material and as catalyst or catalyst support for hydrogenation and isomerisation reactions compared with other ceramic oxides (TiO₂, SiO₂ and Al₂O₃).

ZrO₂ can exist as three polymorphs: monoclinic (M), tetragonal (T) and cubic (C). Theoretically, the valence band of ZrO₂ is formed mainly by O 2p states with some admixing of Zr 4d states, and the conduction band is constructed primarily of Zr 4d states admixed with some O 2p states (French *et al.*, 1994). The Zr 4d states in the conduction band split into two sub-bands upon the increasing symmetry of the crystal structure from the monoclinic to the tetragonal and to the cubic form (French *et al.*, 1994). Based from calculation, the bandgap of monoclinic, tetragonal and cubic ZrO₂ are computed to be 3.12-5.4 eV, 4.10-13.3 eV and 3.2-12.3 eV respectively (Chang & Doong, 2007). The bandgap of ZrO₂ obtained from experimental technique is still controversial because of different microstructures, method of formation and chemical composition of ZrO₂ obtained give different values.

Cubic ZrO₂ is stable from 2370°C to the melting point (2680±15°C). It has a fluorite type crystal structure in which each Zr is coordinated by eight equidistant oxygens and each oxygen is tetrahedrally coordinated by four Zr atoms. Tetragonal ZrO₂ is stable between about 1170°C and 2370°C and monoclinic is stable at all temperatures below 1170°C (Subbarao 1981). Monoclinic is the room temperature

phase. This phase, however do not have many interesting properties in electronic, electrochemical or photochemical applications hence the cubic or tetragonal ZrO₂ must be stabilized at room temperature.

To investigate the energy gap of ZrO₂ experimentally, two techniques are often used: photoluminescence and UV-Visible spectroscopy. Berlin *et al.*, (2012) described three kinds of processes responsible for the luminescence of ZrO₂: (i) band to band recombination (ii) recombination at impurity levels and (iii) recombination at intrinsic defects. From the band to band luminescence band gap of ZrO₂ can be determined.

High temperature phases of cubic and tetragonal ZrO₂ can be stabilized at room temperature either by adding suitable dopants (Garvie 1965) or by reducing the particle size into the nanometer regime. The stabilization of cubic or tetragonal in spherical ZrO₂ powder with diameter in nanoscale has attracted considerable interest in recent years. Chraska *et al.*, (2000) found that any coarsening above a certain critical size results in particle transformation of stabilized high temperature phases to the monoclinic phase. The critical size, up to which the tetragonal phase is stable, is reported to be around 18 nm in diameter. Shukla & Seal (2005) have provided a comprehensive review on the effect of the size of ZrO₂ nanoparticles on the stabilization of tetragonal (T) or cubic (C) phase. According to Shukla & Seal the critical size to stabilized T or C is below 10 nm. Various explanation have been proposed for the observed stabilization of high temperature T or C phase in ZrO₂ particles at room temperature and controversy still exist in the elucidation of the mechanism for such stabilization.

Similar to TiO₂, determination on the phases in ZrO₂ has been done by XRD method. However when ZrO₂ is in nanoscale, XRD has a limitation since peaks from

the XRD of nano-sized particles are very broad. Raman spectra can be used to investigate ZrO₂ nanoparticles. Raman shifts for T-ZrO₂ are reported at 147, 270, 314, 480 and 642 cm⁻¹. Broad band of 177-188 cm⁻¹ the characteristic for M- ZrO₂ and peaks at 350 and 470cm⁻¹ also belong to M-ZrO₂. Raman shift for C-ZrO₂ is at 633cm⁻¹ (Kontoyannis & Orkoula, 1994) and several authors reported that C-ZrO₂ has a rather amorphous-like Raman spectrum with broad band at approximately 530-670 cm⁻¹. This is due to the symmetry of cubic phase. HRTEM has also been used to investigate the crystallinity of nanoparticles of ZrO₂ (Tahir *et al.*, 2007). Crystallinity can be identified by looking at lattice fringes in the HRTEM image. The lattice fringes can provide information of the d spacing (d_{hkl}) of the phase (Lee *et al.*, 2006; Tahir *et al.*, 2007) .

Similar to TiO₂, ZrO₂ as photocatalysts can be applied in environment purification as it can decompose toxic and organic compounds in polluted water and air. Sayama & Arakawa (1993) reported on the successful photocatalytic decomposition of water and the photocatalytic reduction of CO₂ on ZrO₂. They claimed that the oxide semiconductor has a wide band gap and highly negative flat-band potential which is adequate in water splitting process.

The photocatalytic mechanism of ZrO₂ is summarized by Botta *et al.*, (1999) for oxidative degradation of nitrate and EDTA and the reduction of Cr (IV). The mechanism are similar to that of TiO₂ whereby, the oxide need to adsorb water, splitting it then the hydroxyl ion (OH⁻) will need to react with holes to produce the radicals. Works on splitting of water on ZrO₂ has been carried out by Reddy *et al.*, in 2003b. According to Reddy, T and M-ZrO₂ can successfully split water with contribution of T-ZrO₂ is slightly better compares to M-ZrO₂.

Work on ZrO₂ as photocatalyst was also reported by Karunakaran & Senthilvelan in 2005 for the oxidation of aniline. Nanocrystalline ZrO₂ for degradation of Rhodamine dye was done by Zheng *et al.*, (2009). Both works used ZrO₂ in particles form. Whilst, for ZrO₂ nanotubes, there are not many has been done apart from Zhao *et al.*, (2011) and Wang *et al.*, (2012) for the degradation of MO and alcohol respectively.

2.2.1.3 Properties of WO₃

Tungsten trioxide (WO₃) is used for many purposes in everyday life. It is frequently used in industry to manufacture tungstates for x-ray screen phosphors, for fire proofing fabrics and in gas sensors. Due to its rich yellow colour, WO₃ is also used as pigment in ceramics and paints. In recent years, WO₃ has been employed in the production of electrochromic windows, or smart windows. These windows are electrically switchable glass that change light transmission properties with an applied voltage (Deb 2008). This allows the user to tint their windows, changing the amount of heat or light passing through. WO₃ is an n-type, indirect band gap semiconductor with a band gap of 2.6 eV (Yang *et al.*, 2009).

WO₃ has been extensively studied as electrochromic materials because they exhibit high coloration efficiency and high cyclic stability compared to other transition metal oxides. Moreover, WO₃-based devices exhibit low power consumption, hence provide the basis of their applications in smart windows, reflectance variable mirrors and information displays (Nah *et al.*, 2008). Similar to both TiO₂ and ZrO₂ the crystal structure of WO₃ is temperature dependent. It is tetragonal at temperatures above 740°C, orthorhombic from 330 to 740°C, monoclinic from 17 to 330°C, and triclinic from -50 to 17°C. The most common

structure of WO_3 is monoclinic with space group $\text{P}2_1/\text{n}$. Pure single crystals WO_3 will transform from tetragonal to orthorhombic to monoclinic to triclinic then to monoclinic again as the temperature is lowered from 900 to 189°C (Granqvist 1995). Basically at room temperature WO_3 manifest itself as a monoclinic oxide.

As photocatalysts WO_3 has to be in crystalline phase as reported by Wang *et al.*, (2002) as well as nanoporous structures which has high specific surface area. Whilst, Xin *et al.*, (2009) reported that monoclinic phase displayed the best photocatalytic activity for O_2 evolution. Such crystalline structures can be obtained by anodization process and the crystalline phases can be produced by annealing the obtained structures in air at 400°C. The annealing is needed to form the crystalline phase because the anodized WO_3 is amorphous (Nah *et al.*, 2008).

WO_3 is potentially in photocatalytic degradation of organic compounds including a large fraction of environmental toxins. Many efforts have been done to improve the efficiencies of WO_3 photocatalyst. Metal incorporation or doping is one of the metal-semiconductor modification methods used to improve the photocatalytic ability (Hameed *et al.*, 2004; Dhananjeyan *et al.*, 1997; Seery *et al.*, 2007; Kim *et al.*, 2010).

The formation of $\bullet\text{OH}$ in the presence of WO_3 is reported by two paths (Sánchez Martínez *et al.*, 2011). The first is by reductive path with the participation of electron in the conduction band of WO_3 or by direct oxidation of hydroxide ions by the holes of WO_3 which generated in the valence band during the charge separation. Both mechanisms can operate simultaneously in an aqueous dye solution with the presence of WO_3 . Hence the photocatalytic property of the WO_3 is much depended on the formation of the $\bullet\text{OH}$ as discussed before.

The photocatalytic properties of WO_3 mostly reported using nanoparticles and nanoporous structures. The nanoporous WO_3 is normally formed by anodizing method. Watcharenrong *et al.*, (2008) and Guo *et al.*, (2007) reported on the formation of nanoporous WO_3 . Hydrothermal method is also used by Zhao *et al.*, (2008) to produced WO_3 with nanoporous-walled. The photocatalytic of WO_3 can be used to treat many organic compounds such as dyes and phenol.

2.2.2 Anodic oxidation of transition (valve) metal oxides

When a noble metal is exposed to a solution, it will not oxidized. For a nonnoble metal, it may oxidize depending on the environmental condition it is exposed to. The environmental condition can favor dissolution (solvation) of the oxidized metal cation (active corrosion) or a film will form, usually an insoluble protective cover on the metal (passivation). Passivation reactions involve electrochemical steps and typically resulted in formation of anodic oxide layer. Passivation can reduce corrosion of the underlying metal and this phenomenon has been seen as one of the most important aspect in metal protection. Recently passivation of metal has been manipulated to fabricate thin film oxide. The oxide structures formed may be classified into two types according to the morphology of the anodic layer: compact oxide and porous oxide. Based on the thermodynamics and electrochemical studies, the formation of compact and porous metal oxide can be explained by the reaction free energy balance between the anodization of the metal and the chemical dissolution of the anodic oxide in the electrolyte (Wang *et al.*, 2011). Works defining fundamental of passivation process have been reported by many authors. For examples Sato (1990) defined the passivation of metals results

from the formation of continuous oxide layer on the metal surface and Schmuki (2002) reviewed on the underlying mechanism of metal passivation.

During anodization process, the morphology of the anodic oxide layer depends upon the chemical composition of the anodizing electrolyte and the chosen condition of the electrolysis process. Some electrolyte has little or no dissolving action on the oxide layer so that the anodic process will soon stop, leaving a thin film usually referred as a barrier type oxide. If the electrolyte has some dissolve action, then a porous film is formed and the oxidation process can continue leading to the production of relatively thick oxide. In Figure 2.3 possible morphologies of anodic layer formed by anodization is shown. The compact oxide is shown in Figure 2.3 (a), the disordered/random and ordered porous is shown in Figure 2.3 (b) and (c) respectively. Also the ordered tubular structure is shown in Figure 2.3 (d). The fact that anodization can be done in many different kinds of electrolytes, then the formed anodic oxide will obviously have morphologies dependent on the electrolyte itself. Porous layer can be in highly organized with connected pores or as nanotubular structure i.e. the pore boundaries are dissolved forming discrete nanotubular structure. To get the desired morphology the right electrolyte needs to be selected. Generally, electrolyte containing fluoride and/or very acidic will induce chemical dissolution producing porous oxide in the form of random porous, self-organized porous or self-organized nanotubular structure. Figure 2.4 is a flow chart showing several possible structure of oxide formed by anodization. Passivation of metal surface obviously resulted in the formation of passive film. Passive film is formed from the metal itself when the surface atoms are reacting with the environment components (oxygen and water). The passivation can happen by currentless process both in air or water or anodically in oxidizing electrolyte under application of

external field; this is anodic process. Anodic process required an anode (metal to be oxidized) and a counter electrode (platinum or carbon).

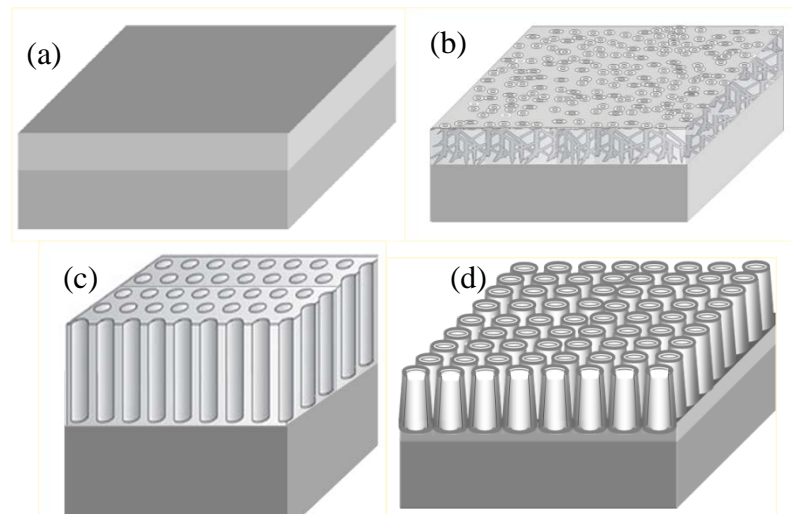


Figure 2.3: Morphologies which can be obtained by electrochemical anodization of metal oxide (a) a compact oxide film (b) a disordered/random nanoporous layer (c) a self-ordered nanoporous layer and (d) a self-ordered nanotubes layer

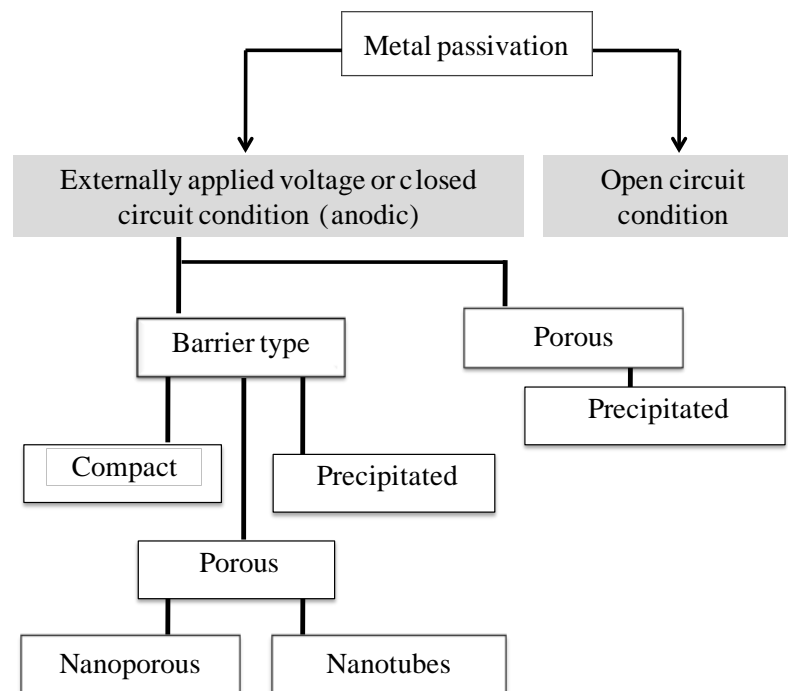


Figure 2.4: Flow chart of metal passivation

It is well documented that the nature of the anodizing process is based upon the electrochemical principle that when current is passed through an electrolyte in which